The 8th European Congress on Computational Methods in Applied Sciences and Engineering
ECCOMAS Congress 2022
5-–9 June 2022, Oslo, Norway

HYBRID HIGH-ORDER FINITE VOLUME DISCONTINUOUS GALERKIN METHODS FOR TURBULENT FLOWS

Dean Yuan[1], Panagiotis Tsoutsanis[1] and Karl W. Jenkins[1]

[1] Cranfield University
Centre for Computational Engineering Sciences, Cranfield University, Cranfield MK43 0AL, UK
dean.yuan@cranfield.ac.uk
panagiotis.tsoutsanis@cranfield.ac.uk
k.w.jenkins@cranfield.ac.uk

Key words: FV, DG, high order methods, turbulent flows, hybrid methods

Abstract. In this paper we develop a family of arbitrarily high-order non-oscillatory hybrid Finite Volume/Discontinuous Galerkin schemes for turbulent flows on mixed-element unstructured meshes. The schemes are inherently compact in the sense that the central stencils employed are as compact as possible, and that the directional stencils are reduced in size, simplifying their implementation. Their key ingredient is the switch between a DG method and a FV method based on the CWENOZ scheme when a troubled cell is detected. Therefore, in smooth regions of the computational domain, the high order of accuracy offered by DG is preserved, while in regions with sharp gradients, the robustness of FV is utilized. This paper also presents the time evolution of troubled cells in unsteady test cases and the use of extended bounds for troubled cell detection. We assess the performance of these schemes in terms of accuracy, robustness and computational cost through a series of stringent 2D and 3D test problems. The results obtained demonstrate the accuracy and robustness that the schemes offer and highlight areas of future improvements that are considered.

1 Introduction

The DG method represents the approximate solution in each element through a piecewise polynomial expansion, avoiding reconstruction on potentially large stencils. The DG method uses many features shared by FV methods, such as the explicit Runge-Kutta time stepping discretization and the use of Riemann solvers at cell interfaces. Similarly, the DG method also suffers from the unphysical oscillations described by the Gibbs phenomenon in the presence of discontinuities. A number of techniques originally developed for the FV method were successfully adapted to the DG method to address this issue, such as the TVB *minmod* slope limiter [1]. The disadvantage of such limiters is the accuracy degradation in smooth flow regions, where the limiter is needlessly activated. WENO schemes use a convex combination of reconstructed polynomials constructed from various directional stencils, such that information is pulled from smooth regions. However, the non-compactness of stencil creates issues for complexity, computational cost, parallelization, and robustness due to the lack of guarantee of finding a stencil in

a smooth region.

In order to alleviate these shortcomings, the Compact WENO (CWENO) scheme, introduced by [2] and extended to mixed-element arbitrary unstructured meshes by [3], uses smaller directional stencils, enhancing the efficiency and robustness of the scheme. Here the directional stencils are contained in the central stencil, and in smooth regions the central stencil order is recovered, whereas in discontinuous regions the chances to have at least a directional stencil with smooth data variation are increased. The CWENOZ method, also [3], is similar but differs in its approximation of the non-linear weights.

Due to their compact size, the CWENO/CWENOZ schemes are more suitable to be used in conjunction with the DG framework. However, in order to preserve the accuracy and compactness properties of the original DG method, the limiting procedure should still be applied only where necessary. For this reason, the limiting strategy usually consists of two steps: first, the so-called *troubled cells*, where a limiting procedure is required, are determined through a troubled cell detector; then, the higher modes of the unlimited DG solution are replaced with the WENO solution, where in order to ensure conservation, the cell average of the new polynomial has to equal that of the DG polynomial.

All the schemes are developed in the open source UCNS3D solver [4], and we assess their performance in terms of robustness, accuracy and computational efficiency for a series of stringent 2D and 3D test problems.

The paper is organized as follows. In Section 2 we introduce the numerical framework used to describe the high-order hybrid DG-FV framework. The numerical results obtained for all the test problems are presented in Section 3 and compared against analytical, reference, or experimental solutions whenever possible. Finally, the last section describes the conclusions drawn from this study.

2 Numerical Framework

2.1 Governing Equations

The compressible 3D Euler equations are considered, written in conservative form as:

$$\frac{\partial \mathbf{U}(\mathbf{x},t)}{\partial t} + \nabla \cdot (\vec{\mathbf{F}}_c(\mathbf{U})) = 0, \tag{1}$$

where $\mathbf{U}$ is the vector of the conserved variables, and $\vec{\mathbf{F}}_c$ are the inviscid and viscous flux vectors given as

$$\mathbf{U} = \begin{bmatrix} \rho \\ \rho u \\ \rho v \\ \rho w \\ E \end{bmatrix}, \vec{\mathbf{F}}_c = \begin{bmatrix} \rho u_n \\ \rho u u_n + n_x p \\ \rho v u_n + n_y p \\ \rho w u_n + n_z p \\ u_n(E+p) \end{bmatrix}, \tag{2}$$

where ρ is the density; u, v, w are the velocity components in x, y and z Cartesian coordinates, respectively, and u_n is the velocity normal to the bounded surface area, defined by $u_n = n_x u + n_y v + n_z w$. Ideal gas is assumed where the total energy per unit mass is calculated by $E = p/(\gamma - 1) + (1/2)\rho(u^2 + v^2 + w^2)$, where p is the pressure, $\gamma = 1.4$ is the ratio of specific heats for air at normal atmospheric conditions.

2.2 Discontinuous Galerkin Method

In DG methods, higher orders of accuracy are attained through a high-order polynomial representation of the local element solution. Consider the unsteady non-linear hyperbolic system of conservation laws on a 3D domain Ω, written in its conservative form:

$$\frac{\partial \mathbf{U}}{\partial t} + \nabla \cdot (\mathbf{F}(\mathbf{U})) = 0, \tag{3}$$

where $\mathbf{U} = \mathbf{U}(\mathbf{x}, t)$ is the vector of conserved variables, $\mathbf{x} = (x, y, z)$ denotes the coordinates of a point of the domain Ω, and $\mathbf{F}(\mathbf{U}) = (\mathbf{f}(\mathbf{U}), \mathbf{g}(\mathbf{U}), \mathbf{h}(\mathbf{U}))$ is the non-linear flux tensor. The physical domain Ω consists of a combination of conforming tetrahedrons, hexahedrons, prisms, or pyramids in 3D; and quadrilaterals or triangles in 2D. All the elements are indexed by a unique mono-index i.

The weak formulation is considered, obtained by multiplying Eq. 3 by a smooth test function $\phi(x)$, integrating over the domain Ω and performing an integration by parts:

$$\int_{\Omega} \phi(\mathbf{x}) \frac{\partial \mathbf{U}}{\partial t} d\Omega + \oint_{\partial\Omega} \phi(\mathbf{x}) F(\mathbf{U}) \cdot n dS = \int_{\Omega} \nabla \phi(\mathbf{x}) \cdot \hat{F}(\mathbf{U}) d\Omega. \tag{4}$$

where $\hat{F}(\mathbf{U})$ is the Riemann flux as employed in FV methods to resolve the non-unique solution at the element boundaries. The solution is discretely approximated by a collection of piecewise solutions on each element, defined as a linear combination of n local polynomial basis functions $B(\mathbf{x})$. The discrete solution lies in a finite-element space of discontinuous functions, i.e. a Sobolev space [5] $V_h = \{\phi_h \in L^{\infty} : \phi_h|_{\Omega} \in V^k(\Omega), k = 0, 1, 2, ..., N\}$, where V^k is the space of polynomials of degree up to k. The discrete solution U_h, with expansion coefficients denoted by u_h, can be seen as expansions over a finite element basis B_j^k in the aforementioned polynomial space, where n is the number of degrees of freedom:

$$\mathbf{U}_h(\mathbf{x}, t) = \sum_{j=1}^{n} u_h(t) B_j^k(\mathbf{x}). \tag{5}$$

In this work a modal formulation is used, i.e. the unknowns to be solved are the polynomial expansion coefficients, with a cell centered Taylor series expansion [6–8]

2.3 Finite Volume

Integrating Eq. (3) over the mesh element i using a high-order explicit finite-volume formulation the following equation is obtained:

$$\mathbf{U}_i^{n+1} = \mathbf{U}_i^n - \Delta t \frac{1}{|V_i|} \sum_{j=1}^{N_f} \sum_{\alpha=1}^{N_{qp}} F^{\mathbf{n_{ij}}} \left(\mathbf{U}_{ij,L}^n(\mathbf{x}_{ij,\alpha}, t), \mathbf{U}_{ij,R}^n(\mathbf{x}_{ij,\alpha}, t) \right) \omega_{\alpha} |S_{ij}|, \tag{6}$$

where $\mathbf{U}_i$ are the volume averaged conserved variables

$$\mathbf{U}_i = \frac{1}{|V_i|} \int_{V_i} \mathbf{U}(x, y, z)\, dV, \tag{7}$$

and $F^{\mathbf{n_{ij}}}$ is a numerical flux function in the direction normal to the cell interface between cell i and the neighbouring cell j, N_f is the number of faces per element, N_{qp} is the number of quadrature points used for approximating the surface integrals, $|S_{ij}|$ is the surface area of the corresponding face, and $\mathbf{U}^n_{ij,L}(\mathbf{x}_{ij,\alpha}, t)$ and $\mathbf{U}^n_{ij,R}(\mathbf{x}_{ij,\alpha}, t)$ are the high-order approximations of the solutions for cell i and cell j respectively; while α corresponds to different Gaussian integration points $\mathbf{x}_\alpha$ and weights ω_α over each face. The volume, surface and line integrals are numerically approximated by suitable quadrature rules, see [9] for details on numerical approximations of multiple integrals.

2.3.1 Reconstruction

For a cell i a high-order polynomial $p_i(x, y, z)$ of order r can be built that provides $r + 1$ order of accuracy, by requiring it to have the same average as a general quantity $\mathbf{U}_i$. This can be formulated as:

$$\mathbf{U}_i = \frac{1}{|V_i|} \int_{V_i} p_i(x, y, z)\, dV. \tag{8}$$

The reconstruction process adopted in `UCNS3D` [4] follows the approaches of Tsoutsanis et al. [3, 10–12], Titarev et al. [13] that have been previously applied to smooth and discontinuous flow problems [3, 4, 10–30] and the reader is referred to previous work [3] which documents the particular CWENO/CWENOZ variant used in this study.

The reconstruction is performed by building a central stencil $\mathcal{S}^1$ by recursively adding neighbouring elements, consisting of $M+1$ cells including the considered cell i. The degrees of freedom a_k for the polynomial for each cell m are obtained by satisfying the condition that the cell average of the reconstruction polynomial $p(\xi, \eta, \zeta)$ must be equal to the cell average of the solution $\mathbf{U}_m$:

$$\int_{V'_m} p(\xi, \eta, \zeta)\, d\xi d\eta d\zeta = |V'_m|\mathbf{U}_0 + \sum_{k=1}^{K} \int_{V'_m} a_k \phi_k\, d\xi d\eta d\zeta = |V'_m|\mathbf{U}_m, \quad m = 1, \ldots, M. \tag{9}$$

and in the present study ψ_k are Legendre polynomials basis functions. Denoting the integrals of the basis function k over the cell m in the stencil, and the vector of right-hand side by A_{mk} and b respectively as given by

$$A_{mk} = \int_{V'_m} \phi_k\, d\xi d\eta d\zeta, \quad b_m = |V'_m|(\mathbf{U}_m - \mathbf{U}_0),$$

the equations for degrees of freedom a_k can be rewritten in a matrix form as:

$$\sum_{k=1}^{K} A_{mk} a_k = b_m, \quad m = 1, 2, \ldots M. \tag{10}$$

The resulting linear system is solved by a QR decomposition based on Householder transformation [31] while using a Moore-Penrose pseudo-inverse of A_{mk} which is only computed once at the beginning of the simulation as detailed in [29].

2.3.2 CWENOZ Scheme

The CWENOZ scheme follows in principle the CWENO scheme, the main difference being the approximation of the non-linear weights. As previously a high-order polynomial is combined with lower-order polynomials arising from the directional stencils also using the Type3 definition as set in [29]. The definition of the optimal polynomial remains the same as before and the CWENOZ reconstruction polynomial is given as a non-linear combination of all the polynomials in the following manner:

$$p(\xi,\eta,\zeta)^{\text{cwenoz}} = \sum_{s=1}^{s_t} \omega_s p_s(\xi,\eta,\zeta), \tag{11}$$

where ω_s correspond to the non-linear weights assigned to each polynomial. The characteristic difference is the approximation of the non-linear weights ω_s. We mentioned previously that the smoothness indicators for the CWENO scheme arise from polynomials of different orders. The WENOZ component of combining unequal degree polynomials as introduced by Borges et al. and Castro et al. [32, 33] is employed in this study, but adapted for unequal polynomials, sized reconstruction stencils and arbitrary elements as has recently been reported by [34, 35] . The non-linear weights are now defined as:

$$\omega_s = \frac{\tilde{\omega}_s}{\sum\limits_{s=1}^{s_t} \tilde{\omega}_s} \quad \text{where} \quad \tilde{\omega}_s = \lambda_s \left(1 + \frac{\tau}{\epsilon + \mathcal{SI}_s}\right). \tag{12}$$

With τ being the universal oscillation indicator and taken as the absolute difference between the smoothness indicators as follows:

$$\tau = \left(\frac{\sum\limits_{s=2}^{s_t} |\mathcal{SI}_s - \mathcal{SI}_1|}{s_t - 1} \right)^b. \tag{13}$$

Similarly to the WENO scheme $\epsilon = 10^{-6}$ is used and $b = 4$. For the present study we employ $r = 1$ for the directional polynomials resulting in 2nd-order of accuracy, and any arbitrary order of accuracy for the polynomial associated with the central stencil. The procedure for the assignment of the linear weights is similar to the CWENO approach described previously.

All the schemes developed are implemented in the UCNS3D CFD code [4], which is written in object-oriented Fortran 2003, employing MPI message passing interface (MPI) and the Open Multi-Processing (OpenMP) application programming interface (API). The reader is referred to [23, 36] for more details on implementation and performance benchmarks. The computational times reported in each case are obtained for the same hardware (and compilation settings) and normalised with respect to a reference setup for the same hardware so that the performance of various algorithms under the same hardware can be appreciated.

The operations performed by the modified version of the UCNS3D code, and used for the present study, are summarized in the flow chart in Fig. 1. As previously mentioned, the UCNS3D code is originally a pure FV code, hence the additional implementation of a modal DG scheme allows the hybridization of the two frameworks, where the unlimited DG solution is checked at

every RK stage of every time step and the FV reconstruction is enabled and substituted to the original DG in the cells that are deemed troubled by the solution checking criteria.

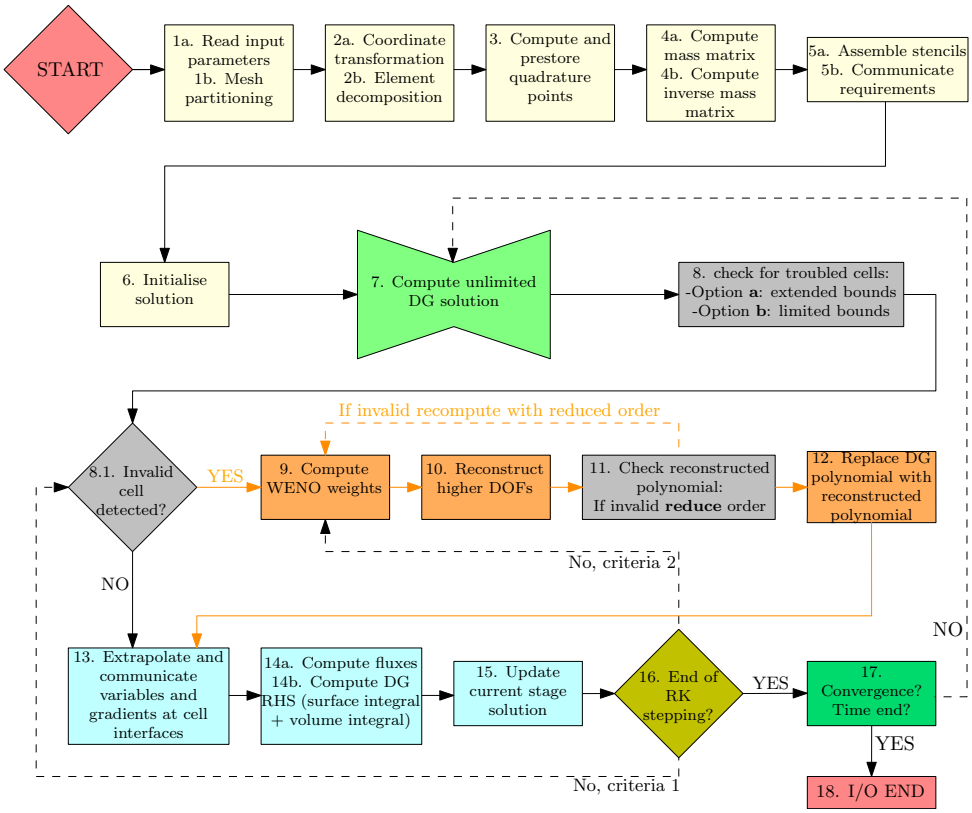

Figure 1: Procedure followed by the hybrid DG-FV scheme

2.4 Troubled Cell Indicators

Following the introduction of WENO type limiting for DG schemes [1, 37], great effort in the recent years was dedicated to the study of troubled cell indicators in order to provide a reliable and efficient system to enable high-order accuracy in smooth regions and non-oscillatory behaviour near discontinuities. These efforts demonstrate that a universal troubled cell detector has still not been achieved. A thorough comparison of the most popular indicators is performed in [38], showing that the best performances were obtained with the KXRCF and Harten's subcell resolution detectors. In this work our main focus is not to compare different detectors, but to demonstrate the viability of utilizing both the FV and DG methods. The detectors used in this work and a brief discussion of their principles follows:

In this work we will adopt the two criteria often used within the MOOD paradigm, namely the Physical Admissible Detector (PAD) and the Numerical Admissible Criteria (NAD), but apply them in an *a priori* fashion. The PAD checks for negative or NaN solutions for the density and pressure variables that of course are not admissible, while the NAD checks that the solution is monotonic and new extrema are not created. The difference when using these kind of indicators

in the context of *a priori* detection is that the neighbouring solutions are compared with the target cell solution at the same time level. The NAD criteria used in this work refers to the DMP-relaxed margins proposed in:

$$\min_{y\in\mathcal{V}_i}(U^n(y)) - \delta \leq U(x) \leq \max_{y\in\mathcal{V}_i}(U^n(y)) + \delta, \tag{14}$$

where the margin δ is defined as:

$$\delta = \max(10^{-4}, \text{par2} \cdot [\max_{y\in\mathcal{V}_i}(U^n(y)) - \min_{y\in\mathcal{V}_i}(U^n(y))]), \tag{15}$$

and the parameter par2 will be taken as 10^{-3}.

2.5 Bounds Definition

An investigation on stencil selection algorithm was conducted in [29], and in [25] the impact of different bounds definitions on the accuracy of MUSCL type scheme demonstrated that considering the direct side neighbouring cells only, is often the reason for reduced order of accuracy. This is due to the activation of the limiter in smooth flow regions which can happen because the bounds imposed by the direct side neighbors provide an extremely narrow range of admissible solutions. This issue is exacerbated by poor quality cells, as the limiter can be activated by the condition number of the resulting reconstruction system. By extending the bounds to the entire stencil, higher orders of accuracy can be maintained.

3 Applications

3.1 Linear Advection Equation

The scheme is first tested for the 2D linear advection of a smooth function $U(x, y, 0) = sin(2\pi x) \cdot sin(2\pi y)$ on a computational domain defined by $[0, 10] \times [0, 10]$ with periodic boundary conditions applied on all sides. Three types of meshes are tested, including a uniform quadrilateral, a triangular, and a hybrid unstructured mesh composed of mixed elements with four different resolutions corresponding to 16, 32, 64 and 128 edges per side. The computations are run for one period $t = 1$ where the e_{L^2} error is computed as follows:

$$e_{L^2} = \sqrt{\frac{\sum_i \int_{\Omega_i} \left(U_e\left(x, t_f\right) - U_c\left(x, t_f\right)\right)^2 dV}{\sum_i |\Omega_i|}}, \tag{16}$$

where $U_c\left(x, t_f\right)$ and $U_e\left(x, t_f\right)$ are the computed and exact solutions at the end of the simulation $t = 1$. The exact solution $U_e\left(x, t_f\right)$ being given by the initial condition itself at $t = 0$. The purpose of this test is to assess the accuracy of the solution obtained with the FV scheme with CWENOZ reconstruction and DG scheme, to be then used as benchmark for the performance of the hybrid FV/DG scheme.

The results are presented in Table 2. Ideally, for this kind of smooth problem the trouble indicator should not detect any troubled cells and the FV should not be activated at all. However, it is typical of trouble indicators to erroneously mark smooth extrema as invalid cells. Indeed this is the case with both the indicators investigated in this test case, i.e. the PAD/NAD detectors

Table 1: Values for e_{L^∞} and e_{L^2} error and convergence rates for smooth profile advection test on a uniform quadrilateral mesh with a hybrid DG-FV scheme when all the cells are artificially rendered troubled, demonstrating that the order of accuracy does not drop due to switching from DG to FV.

DG/CWENOZ all cells troubled	$\mathcal{P}2$				$\mathcal{P}3$				$\mathcal{P}4$			
Number of Edges	e_{L^∞}	$\mathcal{O}_{L^\infty}$	e_{L^2}	$\mathcal{O}_{L^2}$	e_{L^∞}	$\mathcal{O}_{L^\infty}$	e_{L^2}	$\mathcal{O}_{L^2}$	e_{L^∞}	$\mathcal{O}_{L^\infty}$	e_{L^2}	$\mathcal{O}_{L^2}$
16	2.12E-01	-	1.07E-01	-	1.61E-02	-	8.40E-03	-	3.00E-02	-	1.51E-02	-
32	3.12E-02	2.77	1.56E-02	2.78	7.85E-04	4.36	4.28E-04	4.30	1.04E-03	4.85	5.21E-04	4.86
64	4.02E-03	2.96	2.02E-03	2.95	4.21E-05	4.22	2.48E-05	4.11	3.34E-05	4.97	1.66E-05	4.97
128	5.02E-04	3.00	2.51E-04	3.01	2.48E-06	4.08	1.51E-06	4.04	1.05E-06	4.99	5.25E-07	4.99

Table 2: Values for e_{L^2} error and convergence rates for pure FV and DG framework, and hybrid FV/DG with the MOOD_O and Fu troubled cell indicators, for smooth profile advection test. For the hybrid schemes the average percentage of troubled cells are averaged on the total number of time steps and the additional costs for the reconstruction in the troubled cells is quantified though the CPU coefficient normalised with the pure DG computational time on the same mesh and polynomial order.

Order/Number of Edges	FV		DG		DG/MOOD				DG/SD			
Triangular Mesh	e_{L^2}	$\mathcal{O}_{L^2}$	e_{L^2}	$\mathcal{O}_{L^2}$	e_{L^2}	$\mathcal{O}_{L^2}$	% troub. cells	CPU	e_{L^2}	$\mathcal{O}_{L^2}$	% troub. cells	CPU
$\mathcal{P}2/16$	2.14E-02	-	3.38E-05	-	5.96E-04	-	2.61	1.12	9.01E-03	-	20.6	1.19
$\mathcal{P}2/32$	2.92E-03	2.86	2.57E-06	3.72	2.65E-05	4.49	0.70	1.10	1.18E-03	2.94	11.8	1.13
$\mathcal{P}2/64$	3.77E-04	2.95	2.27E-07	3.51	1.09E-06	4.59	0.16	1.08	1.40E-04	3.07	6.48	1.11
$\mathcal{P}2/128$	4.72E-05	2.99	2.83E-08	3.00	1.61E-07	2.77	0.03	1.03	1.55E-05	3.17	3.41	1.07
$\mathcal{P}3/16$	1.39E-03	-	2.26E-06	-	3.50E-04	-	2.66	1.03	1.21E-03	-	74.9	1.29
$\mathcal{P}3/32$	9.60E-05	3.85	8.92E-08	4.67	1.53E-05	4.51	0.70	1.02	6.17E-05	4.30	44.6	1.15
$\mathcal{P}3/64$	6.71E-06	3.84	5.71E-09	3.96	5.44E-07	4.81	0.16	1.03	3.21E-06	4.26	24.0	1.11
$\mathcal{P}3/128$	5.15E-07	3.70	2.92E-10	4.29	1.78E-08	4.93	0.02	1.01	2.73E-07	3.56	12.4	1.09
$\mathcal{P}4/8$	2.85E-02	-	9.78E-07	-	2.49E-03	-	10.6	-	3.84E-02	-	100	1.46
$\mathcal{P}4/16$	1.27E-03	4.49	2.20E-08	5.47	2.86E-05	6.45	2.66	1.04	1.67E-03	4.52	100	1.58
$\mathcal{P}4/32$	4.59E-05	4.79	4.20E-10	5.71	2.79E-07	6.68	0.70	1.03	6.62E-05	4.66	87.8	1.39
$\mathcal{P}4/64$	1.64E-06	4.81	1.74E-11	4.60	2.36E-09	6.89	0.17	1.02	2.97E-06	4.48	65.0	1.26
Hybrid Mesh	e_{L^2}	$\mathcal{O}_{L^2}$	e_{L^2}	$\mathcal{O}_{L^2}$	e_{L^2}	$\mathcal{O}_{L^2}$	% troub. cells	CPU	e_{L^2}	$\mathcal{O}_{L^2}$	% troub. cells	CPU
$\mathcal{P}2/16$	4.52E-02	-	1.58E-04	-	4.18E-03	-	3.31	1.13	1.56E-02	-	22.7	1.20
$\mathcal{P}2/32$	6.08E-03	2.88	2.25E-05	2.81	8.69E-04	2.27	0.87	1.10	1.90E-03	3.04	12.6	1.13
$\mathcal{P}2/64$	7.61E-04	3.01	2.67E-06	3.07	5.03E-05	4.11	0.22	1.02	2.29E-04	3.05	7.06	1.04
$\mathcal{P}2/128$	9.55E-05	2.99	4.30E-07	2.63	1.75E-06	4.85	0.06	1.01	2.64E-05	3.12	3.74	1.03
$\mathcal{P}3/16$	3.49E-03	-	4.22E-06	-	5.15E-04	-	3.42	1.04	3.55E-03	-	85.4	1.27
$\mathcal{P}3/32$	1.62E-04	4.43	4.36E-07	3.28	5.22E-05	3.30	0.85	1.03	1.63E-04	4.45	52.3	1.16
$\mathcal{P}3/64$	1.04E-05	3.96	2.97E-08	3.87	5.06E-07	6.69	0.20	1.07	8.89E-06	4.20	28.4	1.15
$\mathcal{P}3/128$	7.50E-07	3.80	2.04E-09	3.86	3.21E-08	3.98	0.04	1.00	5.90E-07	3.91	14.7	1.05
$\mathcal{P}4/8$	6.39E-02	-	5.13E-06	-	6.66E-03	-	13.9	1.03	9.01E-02	-	100	1.47
$\mathcal{P}4/16$	3.13E-03	4.35	1.61E-07	4.99	1.04E-04	6.00	3.47	1.04	4.76E-03	4.24	100	1.56
$\mathcal{P}4/32$	1.07E-04	4.88	6.06E-09	4.73	1.16E-06	6.49	0.86	1.02	1.69E-04	4.82	91.9	1.36
$\mathcal{P}4/64$	3.37E-06	4.98	2.80E-10	4.44	2.53E-08	5.52	0.20	1.02	6.81E-06	4.63	70.6	1.28

defined in the MOOD paradigm and here simply labelled as MOOD detector, and the shock detector defined as in [39]. We observe a higher rate of convergence in the hybrid scheme due

to the decrease in the percentage of troubled cells due to mesh refinement and the impact on the computational time, compared to the pure DG scheme with the same polynomial order and mesh resolution, here expressed through the CPU coefficient.

3.2 Advection of Discontinuous Profile

The non-oscillatory performances of the hybrid scheme are then assessed against the advection of a discontinuous profile test case. The function is advected for one period $t = 1$ and is in form of a square profile in two dimensions and defined by the following initial conditions:

$$\mathbf{f}(x, y) = \begin{cases} 1, & \text{if } (x, y) \in [0.2, 0.8], \\ 0, & \text{if otherwise.} \end{cases} \tag{17}$$

The computational domain is again given by $[0, 10] \times [0, 10]$ with periodic boundary conditions applied on all sides, and the computations are performed on the uniform and unstructured meshes with a resolution corresponding to 64 edges per side. The results obtained with the pure FV and DG, and with the hybrid FV/DG scheme with the MOOD type indicators with two different threshold values, for the $3^r d$ order of accuracy, are presented in Fig. 2. The trade-off between diffusivity and oscillatory nature can be observed. The pure DG better preserves the initial profile after one period, compared to the pure FV which has a more diffused profile. However, the edges are clearly more oscillatory with the pure DG. In order to dampen the oscillations, the hybrid scheme is tested with two threshold values, i.e. taking a value of par2 = 10^{-3} from the MOOD implementation of [40] and the relaxed value par2 = 10^{-1} from [24]. The indicators will be referred as $MOOD\_O$ and $MOOD\_R$, respectively. In addition, the two bounds definitions discussed in section 2.5 will be used with said indicators, and therefore $MOOD\_O1$ and $MOOD\_R1$ will refer to the extended bounds setting, while $MOOD\_O2$ and $MOOD\_R2$ refers to the version with bounds limited to target cell's direct side neighbours. The $MOOD\_O1$, i.e. lower threshold with extended bounds, seems to be in this case the best compromise to preserve the original accuracy provided by the DG scheme, without producing any oscillation.

The history of the total percentage of troubled cells is plotted in Fig. 3. The configuration with limited bounds results in a higher number of cells marked as troubled, regardless of the selected threshold value. Extending the bounds to the entire stencil and decreasing the threshold value as for the $MOOD\_R1$, results in a smaller amount of invalid cells detected, which is beneficial for the final accuracy but is not sufficient to avoid some oscillations at the edges of the profile.

3.3 Inviscid Taylor-Green Vortex

The ILES of the 3D inviscid Taylor-Green vortex test problem at is employed, for assessing the performance of all the schemes. It is a widely used test problem for the validation of numerical methods, and in particularly at relative coarse-"under-resolved" meshes within the LES context [11, 26, 41–47] due to the pronounced dissipation and dispersion characteristics of non-linear methods. The computational domain is defined as $\Omega = [0, 2\pi]^3$ with periodic boundary conditions. This formulation of the Taylor-Green vortex problem is initialized with the following velocity, density and pressure fields:

$$u(x, y, z, 0) = \sin(kx)\cos(ky)\cos(kz), \tag{18}$$

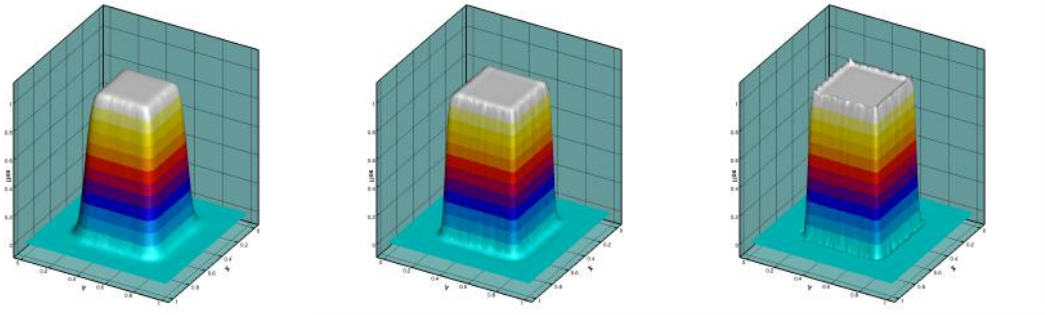

(a) Pure FV hybrid mesh (b) MOOD_O1 hybrid mesh (c) MOOD_R1 hybrid mesh

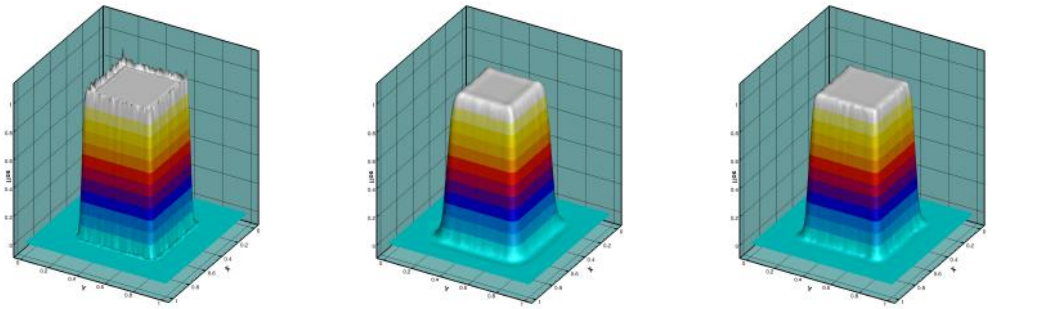

(d) Pure DG hybrid mesh (e) MOOD_O2 hybrid mesh (f) MOOD_R2 hybrid mesh

Figure 2: Computed results for the advection of step profile on a hybrid quad/tri mesh. The performance of the pure FV and DG schemes are compared with the hybrid DG-FV schemes using different troubled cell indicators

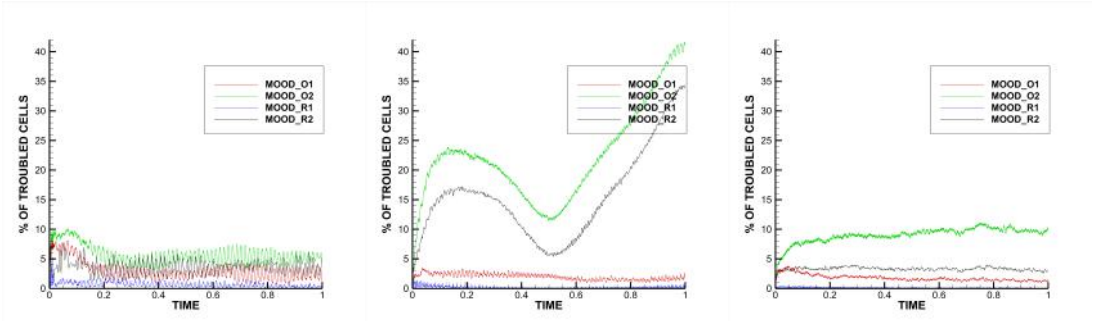

(a) Quadrilateral mesh (b) Triangular mesh (c) Hybrid mesh

Figure 3: Troubled cell history for a advected step profile on various meshes comparing troubled cell indicators

$$v(x, y, z, 0) = -\cos(kx)\sin(ky)\cos(kz), \tag{19}$$

$$w(x, y, z, 0) = 0, \tag{20}$$

$$\rho(x, y, z, 0) = 1, \tag{21}$$

$$p(x, y, z, 0) = 100 + \frac{\rho}{16}[\cos(2z) + 2] \cdot [\cos(2x) + \cos(2y)]. \tag{22}$$

The initial condition corresponds to an initial Mach number $M \approx 0.08$, with wavenumber $k = 2\pi/\lambda = 1$. Simulations were carried out on a hexahedral mesh of 64^3 with four schemes. Two pure FV methods using a 3rd-order and 5th-order spatial CWENOZ schemes, and two hybrid DG-FV of 3rd-order and 4th-order of accuracy. The Shock Detector type indicator is used with the threshold value $C_k = 0.4$. A CFL number of 0.3 is used for the explicit Runge-Kutta 3rd-order scheme, up to $t = 14$ for obtaining the dissipation statistics. The DNS results of Brachet et. al [48] are used for comparisons against the computed solutions.

From the obtained results as shown in Fig. 4 it can be seen from the kinetic energy evolution with time that the hybrid DG-FV method is outperforming the pure FV methods at the same grid resolution, as expected. However, it is clear from the kinetic energy dissipation rate plot that the subject DG implementation is not free from aliasing errors requires either a modal exponential filter, split-form flux approximation, or an overintegration technique, as previously reported by Winters et al [49]. Examining the kinetic energy spectra at time $t = 10.0$, the hybrid DG-FV variant has a substantially better agreement with the theoretical Kolmogorov energy cascade, which is indicative of the low-dissipation properties of the present framework, that can lead to significant improvements in the context of iLES simulations.

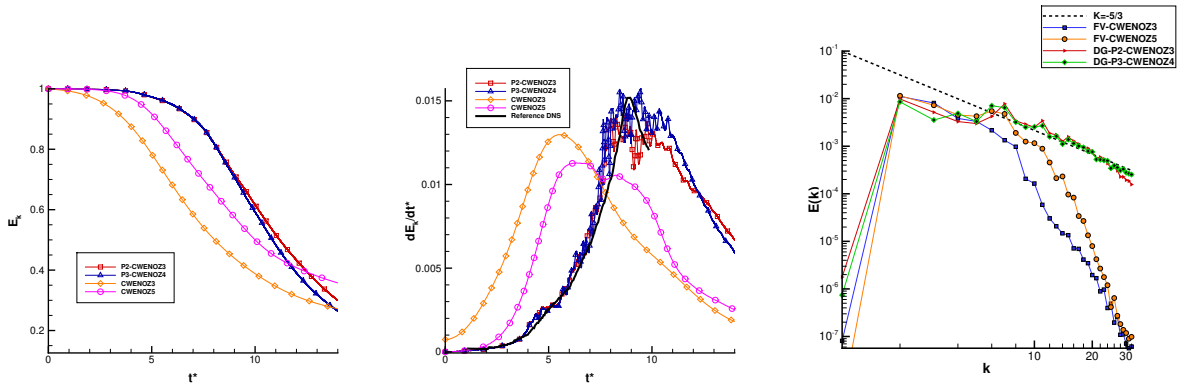

Figure 4: Kinetic energy evolution with time (left), kinetic energy dissipation rate (middle), and kinetic energy spectra (right) at $t = 10.0$ for the subsonic, inviscid Taylor-Green Vortex obtained with various schemes on a 64^3 hexahedral mesh, and comparison with the DNS results of Brachet et al. [48]. DG-FV is superior at the same resolution for kinetic energy evolution and kinetic energy spectra, but the aliasing errors present at the kinetic energy spectra point to improvements required either in the form of modal filter, split-flux, or overintergration.

4 Conclusions

The hybrid DG-FV scheme developed in this paper is able to achieve a high order of accuracy by utilizing the properties of the DG scheme while maintaining robustness and non-oscillatory behavior by transitioning to a FV method. The CWENOZ reconstruction used by the FV method

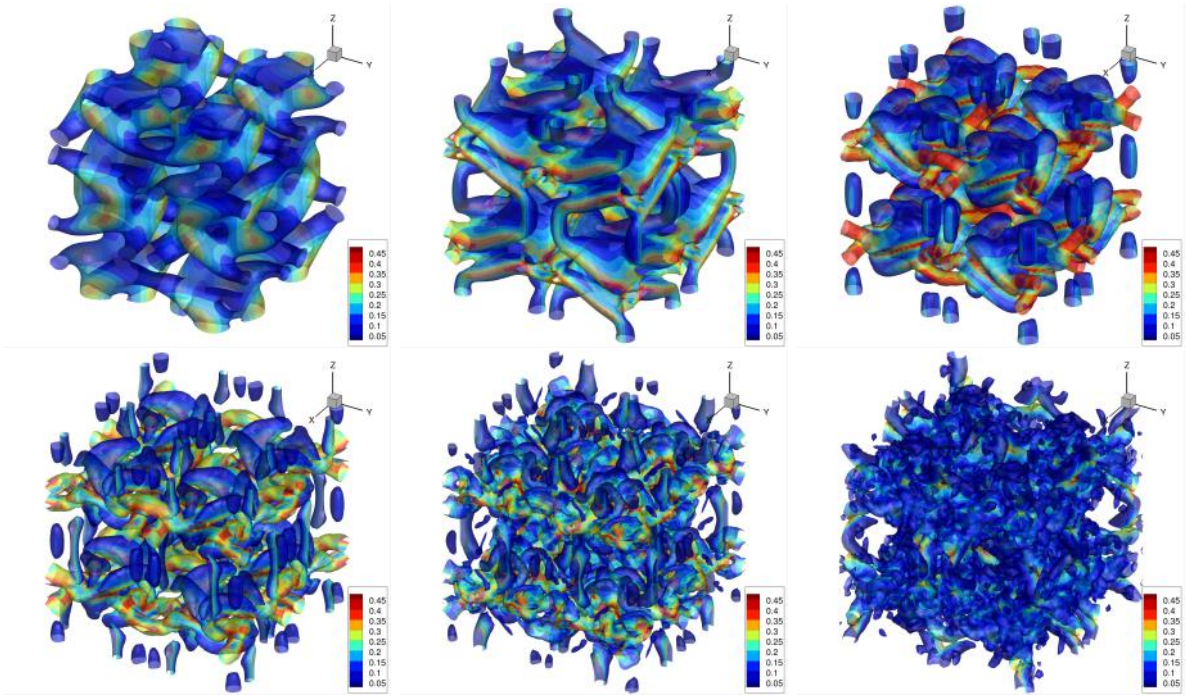

Figure 5: solution of the Taylor-Green vortex flow computed with the DG-P3-CWENOZ4 on a hexahedral mesh of 64^3. The isosurfaces of the Q-criterion Q=2.5, coloured by the kinetic energy are plotted at times $t = 2, 4, 5, 6, 8$ and 10 from top left to bottom right respectively.

is more compact and cost efficient than traditional WENO schemes. The smooth linear advection case shows that the theoretical order of accuracy is attained, discontinuous linear advection case shows the trade-off between diffusivity and oscillations due to choice of bounds and trouble indicator parameter values, and the Taylor-Green vortex case shows the lower dissipation for iLES application. Future work includes development of parameter-free trouble indicators that do not erroneously mark smooth extrema, extension to viscous flows, and application of a modal exponential filter/split flux formulation/overintegration to fix aliasing errors.

REFERENCES

[1] B. Cockburn, C. W. Shu, The Runge-Kutta Discontinuous Galerkin Method for Conservation Laws V, Journal of Computational Physics 141 (2) (1998) 199–224.

[2] D. Levy, G. Puppo, G. Russo, Compact central WENO schemes for multidimensional conservation laws, SIAM Journal of Scientific Computing 22 (2000) 656–672.

[3] P. Tsoutsanis, M. Dumbser, Arbitrary high order central non-oscillatory schemes on mixed-element unstructured meshes, Computer and Fluids 225 (2021). doi:10.1016/j.compfluid.2021.104961.

[4] A. F. Antoniadis, D. Drikakis, P. S. Farmakis, L. Fu, I. Kokkinakis, X. Nogueira, P. A. Silva, M. Skote, V. Titarev, P. Tsoutsanis, Ucns3d: An open-source high-order finite-

volume unstructured cfd solver, Computer Physics Communications 279 (2022) 108453. doi:https://doi.org/10.1016/j.cpc.2022.108453.
URL https://www.sciencedirect.com/science/article/pii/S0010465522001722

[5] D. A. Di Pietro, A. Ern, Mathematical Aspects of Discontinuous Galerkin Methods, Springer Heidelberg Dordrecht London New York, 2011.

[6] H. Luo, J. D. Baum, R. Löhner, A discontinuous Galerkin method based on a Taylor basis for the compressible flows on arbitrary grids, Journal of Computational Physics 227 (20) (2008) 8875–8893. doi:10.1016/j.jcp.2008.06.035.

[7] H. Luo, L. Luo, R. Nourgaliev, V. A. Mousseau, N. Dinh, A reconstructed discontinuous Galerkin method for the compressible Navier-Stokes equations on arbitrary grids, Journal of Computational Physics 229 (19) (2010) 6961–6978. doi:10.1016/j.jcp.2010.05.033.
URL http://dx.doi.org/10.1016/j.jcp.2010.05.033

[8] W. Boscheri, G. Dimarco, High order modal Discontinuous Galerkin Implicit-Explicit Runge Kutta and Linear Multistep schemes for the Boltzmann model on general polygonal meshes, Computers and Fluids 233 (October 2021) (2022) 105224.
URL https://doi.org/10.1016/j.compfluid.2021.105224

[9] A. Stroud, Approximate Calculation of Multiple Integrals, Prentice-Hall Inc., Englewood Cliffs, New Jersey, 1971.

[10] P. Tsoutsanis, V. Titarev, D. Drikakis, WENO schemes on arbitrary mixed-element unstructured meshes in three space dimensions, Journal of Computational Physics 230 (4) (2011) 1585–1601.

[11] P. Tsoutsanis, A. Antoniadis, D. Drikakis, WENO schemes on arbitrary unstructured meshes for laminar, transitional and turbulent flows, Journal of Computational Physics 256 (2014) 254–276.

[12] P. Tsoutsanis, E. M. Adebayo, A. Carriba Merino, A. Perez Arjona, M. Skote, CWENO finite-volume interface capturing schemes for multicomponent flows using unstructured meshes, Journal of Scientific Computing 89 (2021). doi:10.1007/s10915-021-01673-y.

[13] V. Titarev, P. Tsoutsanis, D. Drikakis, WENO schemes for mixed-element unstructured meshes, Communications in Computational Physics 8 (3) (2010) 585–609.

[14] P. Tsoutsanis, D. Drikakis, A high-order finite-volume method for atmospheric flows on unstructured grids, Journal of Coupled Systems and Multiscale Dynamics 4 (2016) 170–186. doi:10.1166/jcsmd.2016.1104.

[15] A. Antoniadis, P. Tsoutsanis, D. Drikakis, Numerical accuracy in RANS computations of high-lift multi-element airfoil and aircraft configurations, in: 53rd AIAA Aerospace Sciences Meeting, Vol. 0317, 2015. doi:10.2514/6.2015-0317.

[16] A. Antoniadis, P. Tsoutsanis, D. Drikakis, High-order schemes on mixed-element unstructured grids for aerodynamic flows, in: 42nd AIAA Fluid Dynamics Conference and Exhibit, Vol. 2833, 2012. doi:10.2514/6.2012-2833.

[17] A. Antoniadis, P. Tsoutsanis, I. Kokkinakis, Z. Rana, D. Drikakis, Azure: An advanced CFD software suite based on high-resolution and high-order methods, in: 53rd AIAA Aerospace Sciences Meeting, Vol. 0813, 2015. doi:10.2514/6.2015-0813.

[18] A. Antoniadis, D. Drikakis, I. W. Kokkinakis, P. Tsoutsanis, Z. Rana, High-order methods for hypersonic shock wave turbulent boundary layer interaction flow, in: 20th AIAA International Space Planes and Hypersonic Systems and Technologies Conference, Vol. 3524, 2015. doi:10.2514/6.2015-3524.

[19] P. Tsoutsanis, I. Kokkinakis, L. Konozsy, D. Drikakis, R. Williams, D. Youngs, Comparison of structured- and unstructured-grid, compressible and incompressible methods using the vortex pairing problem, Computer Methods in Applied Mechanics and Engineering 293 (2015) 207–231. doi:10.1016/j.cma.2015.04.010.

[20] P. Tsoutsanis, H. Srinivasan, Adaptive mesh refinement techniques for high-order finite-volume WENO schemes, in: ECCOMAS Congress 2016, Crete, Greece, 2016. doi:10.7712/100016.2003.8544.

[21] P. Tsoutsanis, N. Simmonds, A. Gaylard, Implementation of a low-Mach number modification for high-order finite-volume schemes for arbitrary hybrid unstructured meshes, in: ECCOMAS Congress 2016, Crete, Greece, 2016. doi:10.7712/100016.2004.8545.

[22] P. Tsoutsanis, D. Drikakis, Addressing the challenges of implementation of high-order finite-volume schemes for atmospheric dynamics on unstructured meshes, in: ECCOMAS Congress 2016, Crete, Greece, 2016. doi:10.7712/100016.1846.8406.

[23] P. Tsoutsanis, A. Antoniadis, K. Jenkins, Improvement of the computational performance of a parallel unstructured WENO finite volume CFD code for implicit large eddy simulation, Computers and Fluids 173 (2018) 157–170. doi:10.1016/j.compfluid.2018.03.012.

[24] P. Farmakis, P. Tsoutsanis, X. Nogueira, WENO schemes on unstructured meshes using a relaxed a posteriori MOOD limiting approach, Computer Methods in Applied Mechanics and Engineering 363 (2020). doi:10.1016/j.cma.2020.112921.

[25] P. Tsoutsanis, Extended bounds limiter for high-order finite-volume schemes on unstructured meshes, Journal of Computational Physics 362 (2018) 69–94.

[26] N. Simmonds, P. Tsoutsanis, A. Antoniadis, K. Jenkins, A. Gaylard, Low-Mach number treatment for finite-volume schemes on unstructured meshes, Applied Mathematics and Computation 336 (2018) 368–393.

[27] F. Ricci, P. Silva, P. Tsoutsanis, A. Antoniadis, Hovering rotor solutions by high-order methods on unstructured grids, Aerospace Science and Technology 97 (2020). doi:10.1016/j.ast.2019.105648.

[28] P. Silva, P. Tsoutsanis, A. Antoniadis, Simple multiple reference frame for high-order solution of hovering rotors with and without ground effect, Aerospace Science and Technology 111 (2021). doi:10.1016/j.ast.2021.106518.

[29] P. Tsoutsanis, Stencil selection algorithms for WENO schemes on unstructured meshes, Journal of Computational Physics: X 4 (2019). doi:10.1016/j.jcpx.2019.100037.

[30] A. F. Antoniadis, P. Tsoutsanis, D. Drikakis, Assessment of high-order finite volume methods on unstructured meshes for rans solutions of aeronautical configurations, Computers and Fluids 146 (2017) 86–104. doi:https://doi.org/10.1016/j.compfluid.2017.01.002.

[31] G. W. Stewart, Matrix Algorithms, Volume 1: Basic Decompositions, Society for Industrial and Applied Mathematics SIAM, 1998.

[32] R. Borges, M. Carmona, B. Costa, W. Don, An improved weighted essentially non-oscillatory scheme for hyperbolic conservation laws, Journal of Computational Physics 227 (2008) 3191–3211.

[33] M. Castro, B. Costa, W. Don, High order weighted essentially non-oscillatory WENO-Z schemes for hyperbolic conservation laws, Journal of Computational Physics 230 (2011) 1766–1792.

[34] J. Zhu, J. Qiu, New finite volume weighted essentially nonoscillatory schemes on triangular meshes, SIAM Journal of Scientific Computing 40 (2018) A903–A928.

[35] J. Zhu, C.-W. Shu, A new type of third-order finite volume multi-resolution WENO schemes on tetrahedral meshes, Journal of Computational Physics 406 (2020) 109212.

[36] P. Tsoutsanis, Knl performance comparison UCNS3D, ARCHER performance report (2017) 157–170.
URL www.archer.ac.uk/community/benchmarks/archer-knl/KNLperfUCNS3D.pdf

[37] J. Qiu, C.-W. Shu, Runge-kutta discontinuous galerkin method using weno limiters, SIAM J. Scientific Computing 26 (2005) 907–929. doi:10.1137/S1064827503425298.

[38] J. Qiu, C. Shu, A comparison of troubled cell indicators for Runge-Kutta discontinuous Galerkin methods using WENO Limiters, SIAM J. Sci. Comput 27 (2005) 995–1013.

[39] G. Fu, C. W. Shu, A new troubled-cell indicator for discontinuous Galerkin methods for hyperbolic conservation laws, Journal of Computational Physics 347 (2017) 305–327. doi:10.1016/j.jcp.2017.06.046.
URL http://dx.doi.org/10.1016/j.jcp.2017.06.046

[40] S. Diot, S. Clain, R. Loubére, Improved detection criteria for the multi-dimensional optimal order detection (MOOD) on unstructured meshes with very high-order polynomials, Computers and Fluids 64 (2012) 43–63. doi:10.1016/j.compfluid.2012.05.004.

[41] D. Drikakis, C. Fureby, F. Grinstein, D. Youngs, Simulation of transition and turbulence decay in the Taylor-Green vortex, Journal of Turbulence 8 (2007) 1–12.

[42] J. Bull, A. Jameson, Simulation of the Taylor-Green vortex using high-order flux reconstruction schemes, AIAA Journal 53 (9) (2015) 2750–2761.

[43] M. Dumbser, I. Peshkov, E. Romenski, O. Zanotti, High order ADER schemes for a unified first order hyperbolic formulation of continuum mechanics: Viscous heat-conducting fluids and elastic solids, Journal of Computational Physics 314 (2016) 824–862.

[44] J.-B. Chapelier, M. de la Llave Plata, E. Lamballais, Development of a multiscale LES model in the context of a modal discontinuous Galerkin method, Computer Methods in Applied Mechanics and Engineering 307 (2016) 275–299.

[45] A. Sifounakis, S. Lee, D. You, A conservative finite volume method for incompressible Navier-Stokes equations on locally refined nested cartesian grids, Journal of Computational Physics 326 (2016) 845–861.

[46] C.-W. Shu, W.-S. Don, D. Gottlieb, O. Schilling, L. Jameson, Numerical convergence study of nearly incompressible, inviscid Taylor-Green vortex flow, Journal of Scientific Computing 24 (1) (2005) 569–595.

[47] B. Vermeire, F. Witherden, P. Vincent, On the utility of GPU accelerated high-order methods for unsteady flow simulations: A comparison with industry-standard tools, Journal of Computational Physics 334 (2017) 497–521.

[48] M. Brachet, D. Meiron, B. Nickel, R. Morf, U. Frisch, S. Orszag, Small-scale structure of the Taylor-Green vortex, Journal of Fluid Mechanics 130 (1983) 411–452. doi:10.1017/S0022112083001159.

[49] A. Winters, R. Moura, G. Mengaldo, G. Gassner, S. Walch, J. Peiro, S. Sherwin, A comparative study on polynomial dealiasing and split form discontinuous galerkin schemes for under-resolved turbulence computations, Journal of Computational Physics 372 (2018) 1–21. doi:10.1016/j.jcp.2018.06.016.